https://doi.org/10.1038/s44310-025-00100-6

Compact potential sensor for spacecraft based on a silicon photonic waveguide

Kosei Otsuka[1], Wataru Takahama[1,2], Rikuto Hojo[3], Takeki Higashiguchi[1], Kazuya Kikunaga[4], Tomofumi Mogami[5], Kazuhiro Toyoda[3] & Yasushi Takahashi[1,2] ✉

Satellites charge up due to incoming electrons and ions, resulting in an electrical potential difference (ΔV) between the satellite and outer space. This can cause electrostatic discharge (ESD) events, damaging electronic devices. To reduce failures due to ESD, sensors monitoring the ΔV can be helpful. Due to spacecraft's restrictions, the sensors should be as small as possible. While small potential sensors in terrestrial applications are often based on electrical conduction in semiconductors, such sensors are not suitable for space application due to a weak resistance to cosmic radiation and ESD. Here, we report a compact sensor based on another sensing method: the utilization of light absorption in a silicon photonic waveguide. We performed experiments in a vacuum chamber simulating the space plasma environment to demonstrate that the light attenuation in the waveguide depends on the ΔV. Our results further indicate that our sensor exhibits a high resistance to ESD.

Over the past decade, the global coverage of services provided by satellites in low Earth orbit (LEO), like high-speed internet and environmental monitoring has rapidly advanced[1–6]. Currently, these services are provided by approximately 10,000 small satellites, and this number is expected to increase further. The development of methods that allow us to reduce failures of satellites is crucial for sustainable space development, as this helps to suppress the increase of space debris and lowers the cost of satellite-based services[7–10]. One of the main causes of failures of satellites is the malfunction of on-board electronic devices. In particular, electronic-device malfunctions triggered by electrostatic discharge (ESD) have been widely reported[11–15], and it has been estimated in 2001 that approximately half of the failures were ESD failures[16]. In today's space industry, which is dominated by commercial satellites, it is difficult to estimate the number of ESD-related incidents, but ESD is still considered the main cause of spacecraft failures.

The primary cause of ESD events in spacecraft is the potential difference that arises between the spacecraft and the surrounding plasma (Fig. 1a). As shown in Fig. 1b, the Earth's plasmasphere contains electrons and ions with densities in the range of approximately 10^4–$-10^6/\mathrm{cm}^3$. This plasma as well as cosmic radiation consisting of high-energy electromagnetic waves and high-energy particles from the Sun can electrify spacecraft[11–21]. As a result, the electrical potential of a satellite (or the floating potential) differs from that of the outer space (the plasma potential), and we denote this electrical potential difference by ΔV. Typically, most of the metallic parts of a spacecraft are electrically connected to the negative terminal of the solar panels, making ΔV negative in general. The density of the plasma in LEO (and also the intensity of the cosmic radiation) can vary by more than an order of magnitude, and accordingly ΔV can also vary significantly. If $|\Delta V|$ becomes large (e.g., $\Delta V < -100$ V), the risk of an ESD failure will increase since usually not all parts of the satellite charge up to the same voltage[22]. However, only a few measurements of such ΔV-fluctuations experienced by spacecraft have so far been reported[23–25], and thus the details of the mechanisms of ESD failures are still unclear, making quantitative risk assessment difficult[26–28]. To reduce ESD failures, sensors capable of monitoring ΔV can be helpful, and due to the size and weight restrictions of spacecraft, they should be as small as possible.

Unfortunately, achieving accurate measurements of electrical potential differences experienced by spacecraft using so-called potential probes remains challenging due to disturbances from the surrounding plasma and self-electrification[29]. Moreover, they are typically relatively large, which makes it difficult to install them on small spacecraft[30]. While certain types of surface potential meters (which are widely used in terrestrial applications) have the advantage that they are compact, highly sensitive, and do not consume much power, their sensing mechanism (which is based on evaluating changes in the electrical conduction) lacks radiation resistance, which limits the lifespan in space[31]. Furthermore, the surface potential meter itself can suffer damage in the case of an ESD event. A small ΔV-sensor for spacecraft that uses another phenomenon than electrical conduction would be therefore advantageous.

[1]Department of Physics and Electronics, Osaka Metropolitan University, Osaka, Japan. [2]Faculty of Environmental, Life, Natural Science and Technology, Okayama University, Okayama, Japan. [3]Department of Space Systems Engineering, Kyushu Institute of Technology, Kitakyushu, Japan. [4]Sensing Technology Research Institute, National Institute of Advanced Industrial Science and Technology, Tosu, Japan. [5]Electrostatic Engineering DEPT, Kasuga Denki INC, Kawasaki, Japan. ✉e-mail: y-takahashi@okayama-u.ac.jp

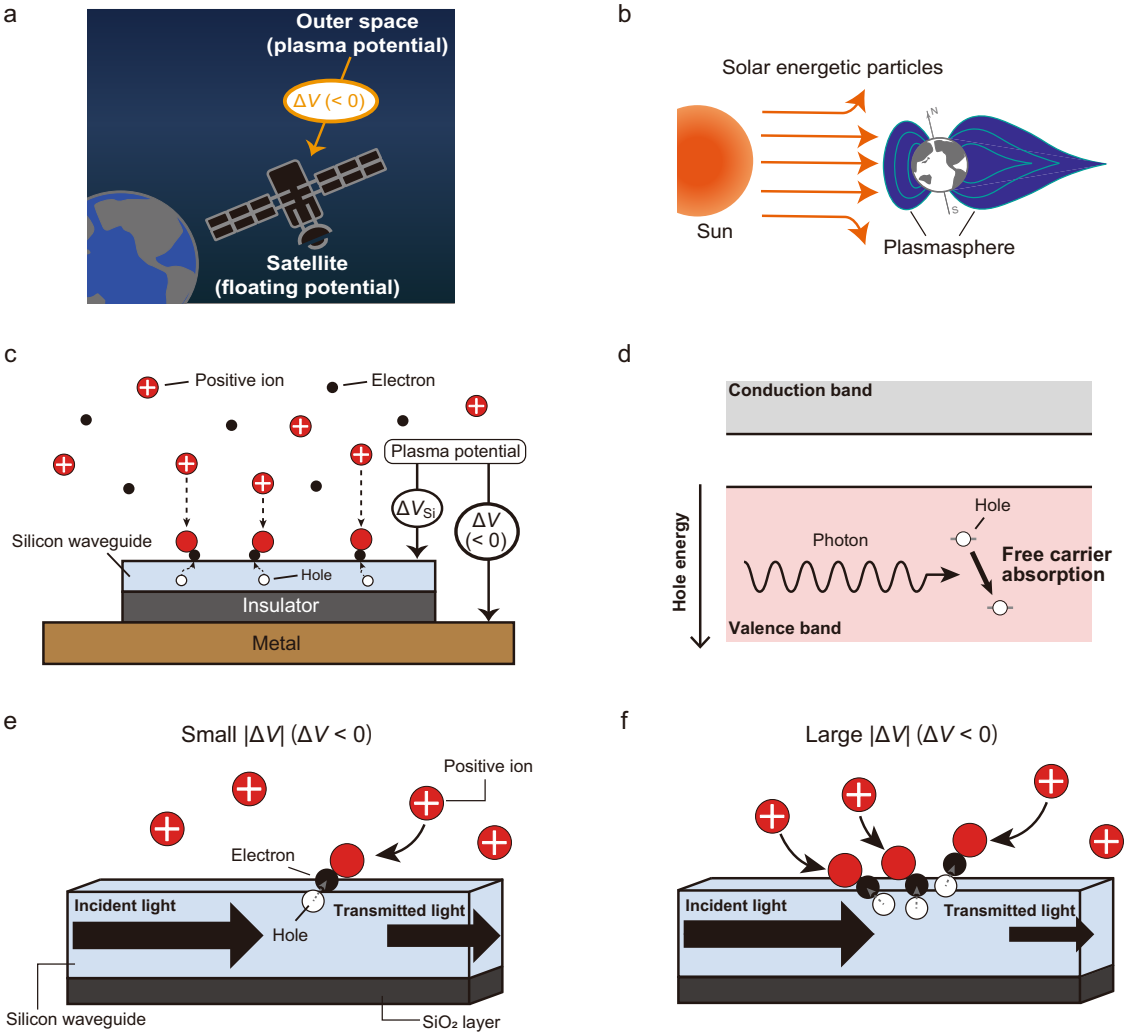

Fig. 1 | Principle of measuring ΔV using a silicon photonic waveguide. **a** Illustration of the potential difference between a spacecraft and the surrounding plasma, ΔV. As the metallic components of a satellite are typically connected to the negative terminal of the solar panels, ΔV is negative in general. **b** Illustration of plasma in the Earth's plasmasphere and high-energy particles from the Sun, which can cause spacecraft electrification. **c** Definitions of the considered potential differences: the potential difference between the silicon layer (light blue) and the surrounding plasma, ΔV_{Si}, and the potential difference between the base metal plate (brown) and the surrounding plasma, ΔV. In the case that ΔV (and ΔV_{Si}) is negative, positive ions in the plasma are pulled toward the metal plate and the silicon layer, and thus positive charges are also transferred to the silicon layer. Due to the insulating layer (gray), the transferred charges accumulate in the silicon layer, and this charging process continues until ΔV_{Si} reaches zero. **d** Diagram of an FCA process in a semiconductor, where a hole absorbs a photon propagating through the semiconductor. **e**, **f** Light attenuation due to FCA in the silicon photonic waveguide in the case of small and large negative ΔV values, respectively.

Here, we present a small ΔV-sensor for spacecraft that uses the phenomenon of charge-induced light absorption in a silicon photonic waveguide. We demonstrate its operation using a vacuum chamber that simulates a space environment and investigate the device characteristics.

Results

Measurement principle

Our device makes use of the self-electrification of the spacecraft induced by the surrounding plasma. Fig. 1c is used to clarify the charge transfer process from the surrounding plasma consisting of electrons (shown in black) and positive ions (red) to a silicon layer with a photonic-crystal waveguide structure (light blue). The metal plate (brown) represents the satellite's outer shell. The chip containing the silicon layer with the photonic waveguide also has an insulating layer (gray), which suppresses the escape of the charges transferred to the silicon layer. In the case that ΔV is negative (which corresponds to the situation in Fig. 1a), positive ions are pulled toward the silicon layer. When positive ions reach the silicon surface, they can receive electrons, resulting in the generation of holes within the silicon layer (which is equivalent to a transfer of positive charges to the silicon layer). Since the hole density in the silicon layer increases with time, the potential difference between the silicon layer and the surrounding plasma (ΔV_{Si}) starts to deviate from ΔV. The transfer of positive charges to the silicon layer continues until the potential of the silicon layer equals the plasma potential, i.e., $\Delta V_{Si} = 0$ V. Consequently, the final hole density in the silicon layer (N_{hole}) is proportional to ΔV, which can be expressed as

$$N_{hole} = A\Delta V + B \quad (1)$$

where the coefficient A depends on the properties of the silicon chip and exhibits different values for positive and negative ΔV. The y-intercept B should ideally be zero; however, due to the interaction of the silicon with the plasma, it can remain finite.

As shown in Fig. 1d, the holes transferred to the silicon layer absorb a fraction of the light propagating through the photonic-crystal waveguide structure by free carrier absorption (FCA)[32–35]. The absorption coefficient of FCA (α_{FCA}) by the transferred holes is proportional to the N_{hole} according to

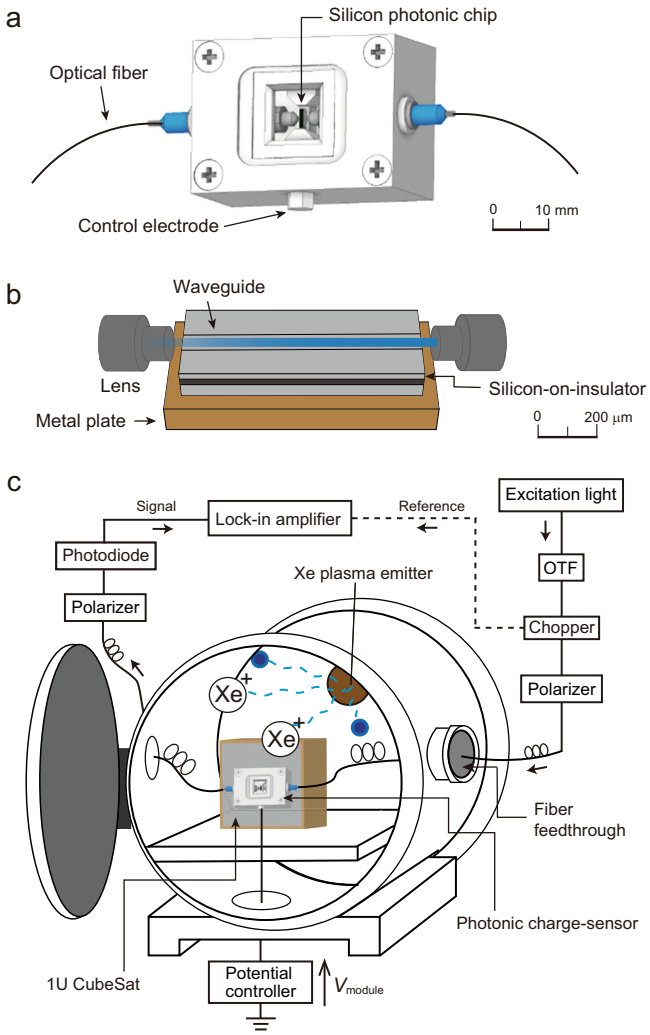

Fig. 2 | Photonic charge sensor and experimental setup. a Schematic of the photonic charge sensor used in the experiment. **b** Enlarged view of the silicon photonic chip shown in Fig. 2a. Integrated small aspheric lenses allow us to achieve highly efficient coupling between the optical fibers and the waveguide, and these lenses are fixed to the housing by metal brackets. **c** Schematic of the experimental setup used to demonstrate the photonic charge sensor. The vacuum chamber is equipped with an Xe plasma emitter, and the sensor module is mounted on the side face of a 1U CubeSat mock-up. The potential controller outside the chamber controls the voltage of the module, V_{module}. The excitation light source and the light detection system (a photodiode and a lock-in amplifier) are also located outside the chamber. OTF optical tunable filter.

the following relation[36,37].

$$\alpha_{FCA} = N_{hole}\sigma_{FCA} \quad (2)$$

where σ_{FCA} is the absorption cross section for FCA. The transmitted light intensity ($I_{\Delta V}$) decreased by FCA is then evaluated using

$$I_{\Delta V} = I_0 \exp\left(-\alpha_{FCA} n_{wg} L\right) \quad (3)$$

where I_0 is the intensity for $\Delta V = 0$ V, L is the waveguide length, and n_{wg} is the enhancement factor based on the effective refractive index of the waveguide[37]. Therefore, the value of ΔV in Fig. 1c can be estimated from the attenuation $I_{\Delta V}/I_0$ of the light propagating through the waveguide. If $|\Delta V|$ is small (for example, $\Delta V = -100$ V), the N_{hole} is low, resulting in weak attenuation (Fig. 1e). If $|\Delta V|$ is larger (for example $\Delta V = -250$ V), the N_{hole} is higher, leading to stronger attenuation (Fig. 1f). Since this mechanism does not rely on the electrical conduction in the used semiconductor material, it should be highly resistant to ESD.

Device design and experimental setup

Figure 2a shows the fiber module used for the demonstration of this type of sensor. The silicon photonic waveguide chip is positioned at the center of the module and is attached to the metal plate using an adhesive. Light from a single-mode fiber is focused on the right edge of the photonic crystal waveguide via a lens that is fixed by a metal bracket, and the transmitted light is coupled into another single-mode fiber (see the "Methods" section and the Supplementary Information for details). The components shown in Fig. 2b are enclosed in a stainless-steel housing. The metal plate, the metal brackets, and the housing are electrically connected to the control electrode. The photonic crystal waveguide[38] (with a length of 0.8 mm) was fabricated from a silicon-on-insulator wafer with a 225-nm-thick top silicon layer and a 3-μm-thick SiO_2 layer. The silicon surface of the waveguide is covered by a native oxide film of approximately 1 nm in thickness[39]. The waveguide is designed with sufficient tolerance to guide C-band light (from 1530 to 1565 nm, which is most commonly used in optical communications) even when the temperature of the silicon chip varies within a range of ±100 °C (the photonic-crystal waveguide design and the fabrication method are described in the Supplementary Information and the "Method" section, respectively)[40]. We hereafter refer to this module as a photonic charge sensor.

Figure 2c shows the vacuum chamber used to simulate a space environment using a xenon (Xe) plasma emitter (we also performed an additional experiment using argon (Ar) as the plasma source in a separate vacuum chamber. Selected results obtained with Ar ions are provided in the Supplementary Information). The diameter of the chamber is approximately 1 m, and it is about 1.2 m long[13]. The photonic charge sensor is mounted on a side face of a 1U CubeSat[41] mock-up placed on a polymer stage inside the chamber, and the side with the sensor faces away from the plasma emitter (see the Supplementary Information for details). The potential of the module (V_{module}) is controlled by a potential controller connected to the control electrode. To investigate the characteristics of the photonic charge sensor, Xe plasma was generated inside the chamber and the intensity of the transmitted light was recorded while varying V_{module}. The achieved plasma density was approximately 5.15×10^{11} m^{-3} (which is comparable to the median plasma density in LEO) and the plasma potential (V_{plasma}) was approximately 17 V. ΔV is defined as $V_{module} - V_{plasma}$. Light from an external source was delivered to the module via the optical fiber, and the transmitted light intensity was measured using a photodiode and a lock-in amplifier (see the "Methods" section for details)[37]. In the following analysis of the data, the recorded time traces of the transmitted light intensity are normalized to the average transmitted intensity during the first 30 seconds of each experiment.

Confirmation of the proposed sensing mechanism

We first demonstrate the behavior of the device explained in Fig. 1c using a V_{module} of −100 V. The upper panel of Fig. 3a shows that V_{module} was switched from 0 to −100 V at $t = 150$ s and stayed at this value until $t = 370$ s. The gray-shaded regions (i)–(iii) in the lower panel indicate the time range where Xe plasma was generated, and the red curve shows the recorded device response. In time region (i), $\Delta V = -17$ V and $\Delta V_{Si} < 0$ V, and thus positive ions in the surrounding plasma are pulled toward the metallic components of the sensor (the metal plate, the brackets, and the housing) and the top silicon layer containing the waveguide structure. The transmitted light intensity gradually decreases, because the holes that have been transferred from the positive ions to the top silicon layer (to reduce ΔV_{Si}) absorb a fraction of the light in the waveguide by FCA (Fig. 3b). At $t = 150$ s, the intensity reduction is not yet saturated, that is, $\Delta V_{Si} \neq 0$ (in another measurement run, we confirmed that this reduction saturates after approximately 30 min).

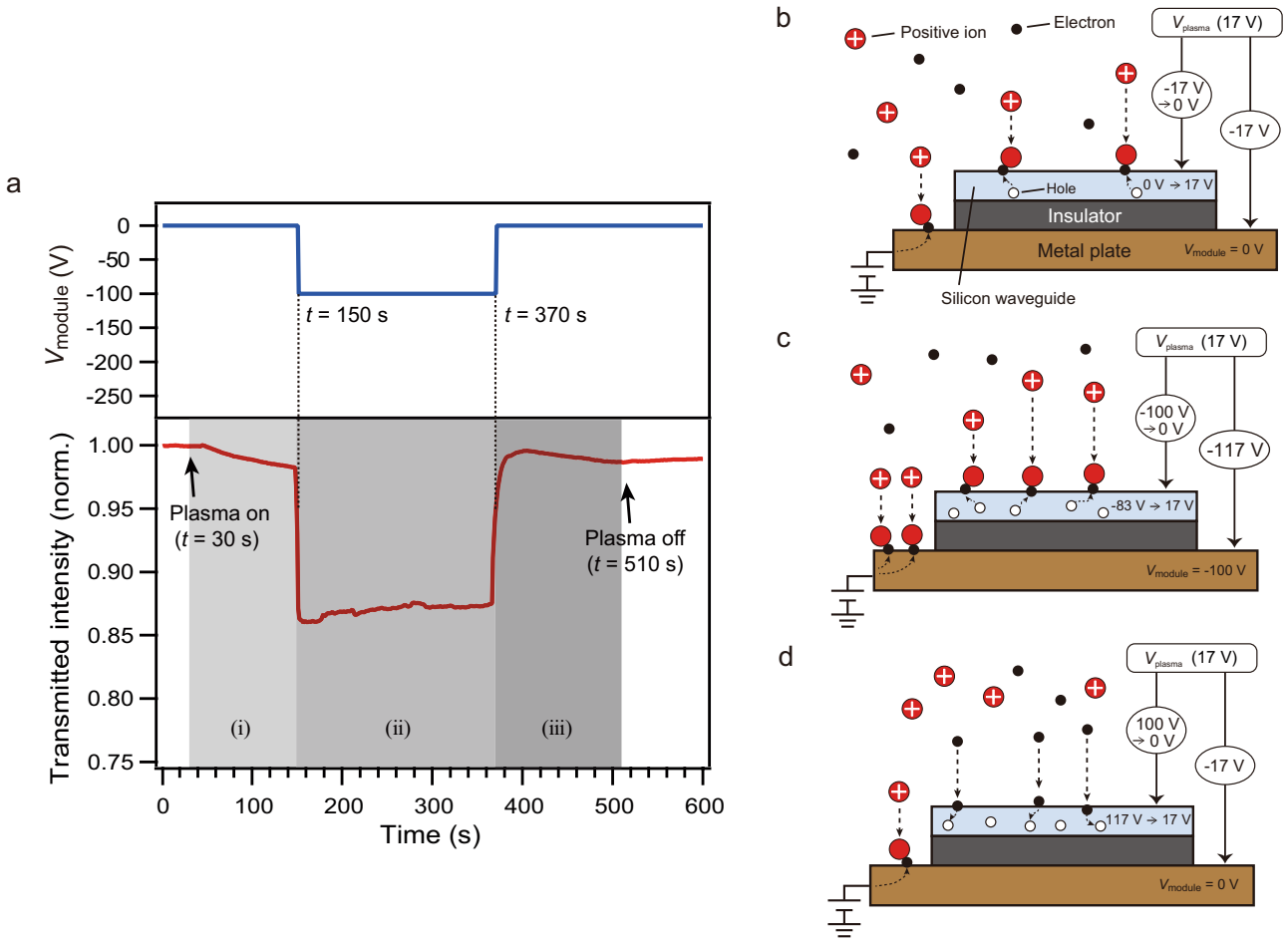

Fig. 3 | Basic response of the photonic charge sensor to a negative ΔV. **a** The applied voltage profile (upper panel) and the recorded device response (lower panel). The three gray-shaded regions denoted by (i)–(iii) indicate different characteristic time regions during plasma generation. **b** The values of ΔV and ΔV_{Si} during time regions (i), where $V_{module} = 0$. In this situation, positive ions are pulled toward the metal plate and the top silicon layer containing the waveguide structure due to the negative ΔV. **c** The values of ΔV and ΔV_{Si} during time region (ii), where $V_{module} = -100$ V. Here, positive ions are strongly pulled toward the metal plate and the top silicon layer due to the large negative ΔV. The positive charges transferred to the top silicon layer absorb a fraction of the light propagating through the waveguide, and thus reduce the transmitted light intensity. **d** The situation during time region (iii), where the top silicon layer is positively charged and $V_{module} = 0$; while positive ions are pulled toward the metal plate, electrons are pulled toward the top silicon layer, and the transmitted light intensity recovers as the electrons recombine with the holes in the top silicon layer.

At $t = 150$ s ($\Delta V = -117$ V and $\Delta V_{Si} = -100$ V), an immediate reduction in transmitted light intensity by approximately 12% is observed. As shown in Fig. 3c, positive ions are pulled toward the silicon layer and generate holes (this process can continue until ΔV_{Si} become zero). Again, the observed reduction in the transmitted light intensity is caused by FCA. After this initial reduction in time region (ii), the transmitted light intensity remains nearly constant because ΔV_{Si} is relatively close to zero. At $t = 370$ s ($\Delta V = -17$ V and $\Delta V_{Si} = +100$ V), the transmitted light intensity starts to recover to a level close to that observed before exposure to the Xe plasma. This recovery in time region (iii) is caused by the reduction of the hole density in the top silicon layer due to recombination with the attracted electrons (Fig. 3d). We repeated this experiment 10 times in a vacuum chamber filled with Ar ions and examined the variation in the magnitude of transmitted light attenuation. The standard deviation at $V_{module} = -100$ V is as low as 0.0034 (see the Supplementary Information).

The data shown in Fig. 4 clarifies that the device response for $|\Delta V| > 50$ V almost follows the theoretical behavior described by Eqs. (1)–(3). Here, we used a different sensor module than that used for Fig. 3, but the device structure was the same. The upper panel in Fig. 4a shows the applied voltage profile: V_{module} was switched from 0 V to a negative target value and then switched back, and the target value was changed from −50 to −200 V in steps of −50 V. The lower panel shows the recorded device response. Note that plasma generation was started well before the start of the experiment, and thus we can consider $\Delta V = -17$ V and $\Delta V_{Si} = 0$ V at $t = 0$ s. We find that the magnitude of the intensity reduction becomes larger as $|\Delta V|$ increases. Fig. 4b plots the minimum transmitted intensity at a given potential step as a function of ΔV (the experimental error estimated from the Ar-ion experiments is described in the Supplementary Information). The red curve using Eqs. (1)–(3) shows that the attenuation closely follows the theoretical fit when $|\Delta V| > 67$ V (see Eq. (S4) in the Supplementary Information for details). These results indicate that the hole density inside the top silicon layer increases as ΔV becomes more negative, making the FCA rate larger. It should be emphasized that the photonic charge sensor can measure the potential difference of $\Delta V < -100$ V, where the ESD risk begins to increase.

The spike-like responses observed for $V_{module} = -200$ V are attributed to discharges in the vacuum chamber, which lead to a short reduction in $|V_{module}|$. We confirmed this assignment using a discharge meter attached to the chamber[13]. Note that, although we repeatedly performed experiments with $V_{module} = -200$ V, the module remained undamaged. This result suggests that the photonic charge sensor is resistant to ESD and can even trace relatively fast fluctuations of ΔV under certain conditions.

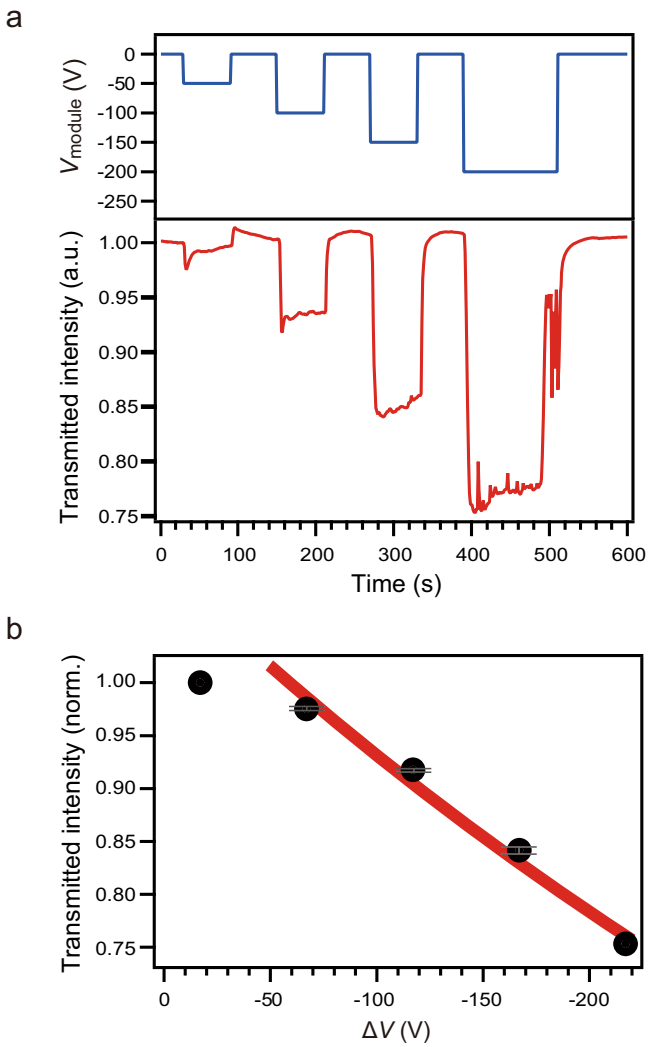

Fig. 4 | Demonstration of monitoring Δ*V*-fluctuations. a The applied voltage profile (upper panel) and the recorded device response (lower panel). Plasma generation started at $t < -1800$ s. When V_{module} was set to −200 V, discharges occurred, resulting in spike-like increases in the transmitted light intensity, but the module remained undamaged. **b** The minimum transmitted light intensity as a function of ΔV to clarify the device response. The red curve is a theoretical fit to the data corresponding to $\Delta V < -67$ V. Error bars are added to the data at $V_{module} = -67$ V, −117 *V*, and −167 V.

Data for more realistic voltage profiles

The upper panel of Fig. 5a shows a voltage profile that better reflects the continuity of usual Δ*V*-variations in space: V_{module} is first decreased stepwise from 0 to −250 V, and then increased back to 0 V. The device response is shown in the lower panel (a sensor module different from the modules used for Figs. 3 and 4 was used). The results of the first half of the experiment resemble those shown in Fig. 4: As V_{module} is decreased, the transmitted light intensity reduces, since the hole density in the top silicon layer increases (Fig. 5a; $t < 700$ s), and the plot of the minimum transmitted intensity as a function of ΔV (Fig. 5b; solid circles) indicates that the attenuation, proportional to $|\Delta V|$, agrees well with the theoretical fit given by Eqs. (1)–(3). For $V_{module} = -250$ V, we can also confirm spike-like responses caused by discharges.

The second half of the experiment is in overall agreement with the behavior discussed above: As V_{module} is stepwise returned to 0 V, the transmitted light intensity increases (since the hole density decreases), and also the plot of the maximum transmitted intensity as a function of ΔV (Fig. 5; open triangles) results in a trend close to that observed in the first half of the experiment. On the other hand, the speed of the response to a change in V_{module} is much slower than that observed in the first half of the experiment. In addition, the experimental error increases. The mechanism for these responses are explained in Fig. 5c, d.

Fig. 5c shows the situation at the time instant indicated by the vertical arrow labeled "A" in Fig. 5a (slightly before the voltage step; $V_{module} = -200$ V and $\Delta V = -217$ V). In this situation, the net charge transfer from the surrounding plasma to the top silicon layer is zero, because the transmitted light intensity is almost stable (ΔV_{Si} is close to 0 V), while positive ions are still accelerated toward the exposed metallic components of the sensor due to the negative ΔV. Figure 5d illustrates how the plasma behaves during the time region indicated by the horizontal double-headed arrow labeled "B" in Fig. 5a after the voltage step to $V_{module} = -150$ V ($\Delta V = -167$ V). Also in this time region, positive ions are accelerated toward the exposed metallic components of the sensor due to the negative ΔV. On the other hand, while we would expect electrons to be strongly pulled toward the top silicon layer if we simply consider ΔV_{Si} (since ΔV_{Si} instantly increased to 50 V due to the increase of V_{module} by 50 V), the effective potential difference between the waveguide and the surrounding plasma including the influence of the surrounding charge distribution (Coulomb repulsion) is relatively low (see Fig. S1 in the Supplementary Information). Therefore, the decrease of the holes in the top silicon layer is slow, resulting in the slow increase of the transmitted light intensity observed in the lower panel of Fig. 5a. In contrast, when V_{module} was changed from −50 to 0 V, no Coulomb repulsion occurred, because $V_{module} = 0$ V. Thus, in the final voltage step, the transmitted light intensity increased immediately like in Figs. 3a and 4a. Regarding the measured transmittance of about 95% for $\Delta V = -67$ V in the second half of the experiment (Fig. 5b), this value clearly deviates from the trend of the other values. We explain this with too early voltage-level switching: V_{module} was changed from −50 to 0 V before ΔV_{Si} reached 0 V. Owing to the slow response, the experimental error increases when ΔV is increased.

The results in Fig. 5 demonstrate that the photonic charge sensor is capable of detecting continuous variations in ΔV. Finally, we also show that this sensor can monitor potential differences for at least an hour. Fig. 6 presents the results that we obtained when V_{module} was set to ≤ −100 V for about one hour (this measurement was carried out subsequent to that of Fig. 5). During the period with $V_{module} = -150$ V (between $t = 60$ and 1800 s), the transmitted light intensity remains nearly constant, and after the voltage step to $V_{module} = -100$ V at $t = 1800$ s, the transmitted light intensity gradually increases and reaches a stable value at around $t = 2600$ s. Slightly after the final voltage step to $V_{module} = 0$ V at $t = 3200$ s, the transmitted light intensity returns to a level close to the initial value.

Discussion

The results shown in Figs. 3–6 indicate that the developed photonic charge sensor is capable of monitoring the ΔV between a spacecraft and the surrounding plasma. The sensing mechanism is based on three facts: (1) through the interaction with the surrounding plasma, free carriers are generated in the silicon layer with the photonic-crystal waveguide structure, (2) the number of free carriers is proportional to $|\Delta V|$, and (3) the intensity of the light propagating through the waveguide is reduced by FCA. The main advantage of this type of sensor is that only light absorption by free carriers is used to determine ΔV. It does not rely on evaluating changes in the electrical conduction, and as a result, the sensor should exhibit good resistance to discharges, as indicated in Figs. 4a and 5a.

The density of holes in the silicon waveguide induced by ΔV is estimated from the attenuation of the transmitted light[37]. The hole density in time domain (ii) of Fig. 3a is 2.97×10^{17} cm^{-3} (see the Supplementary Information for details). The 25% attenuation observed at $V_{module} = 200$ V in Fig. 4a is caused by holes with a density of 5.58×10^{17} cm^{-3} (see Fig. S8 for the carrier density for each V_{module}). Silicon crystals can maintain their structural integrity up to the carrier density of 1.0×10^{20} cm^{-3}. Therefore, the silicon waveguide for the photonic charge sensor will not be deteriorated by carriers induced by a ΔV of several hundred V.

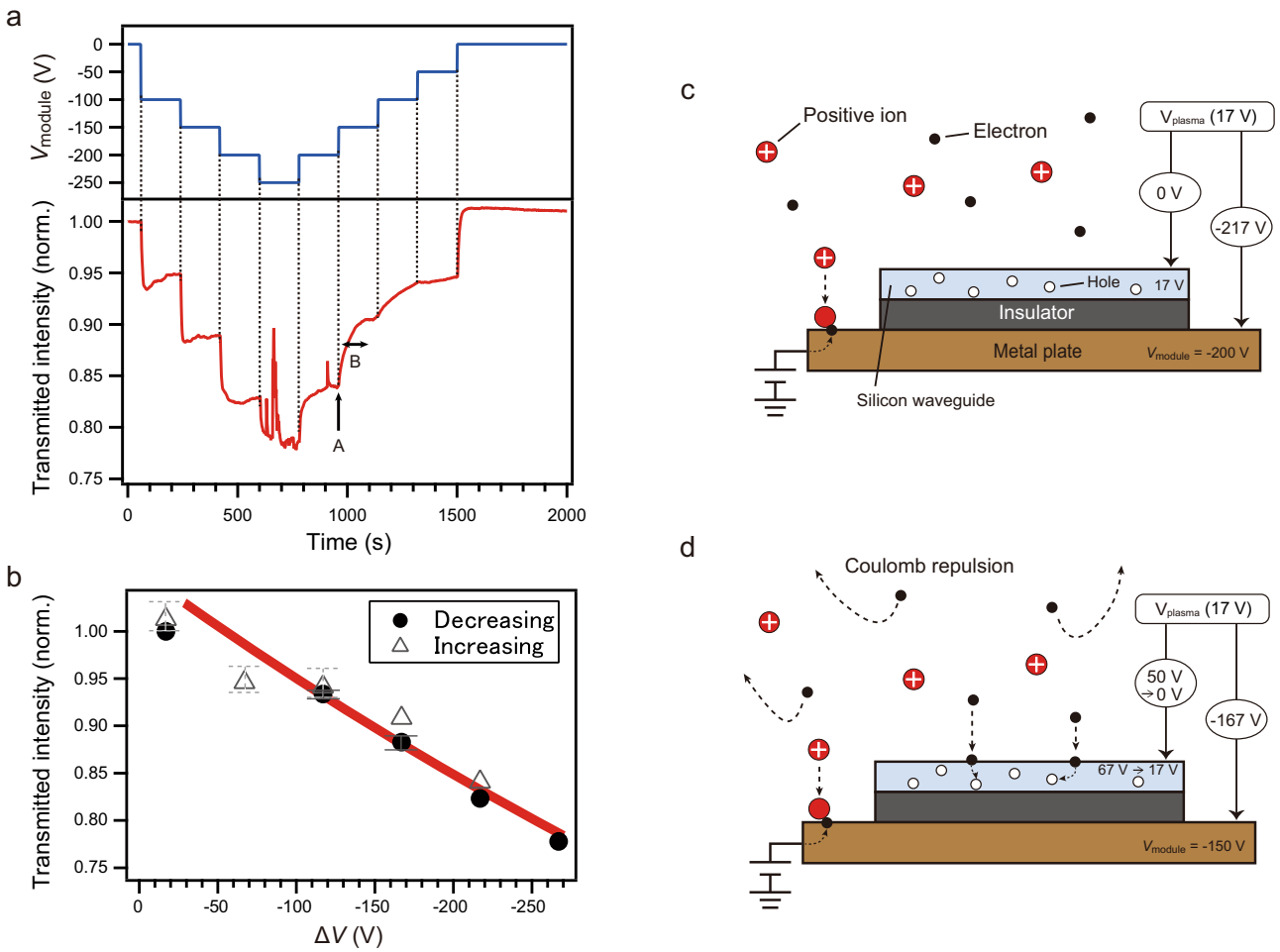

Fig. 5 | Demonstration of monitoring continuous ΔV-variations. a The applied voltage profile (upper panel) and the device response (lower panel). In the first half of the experiment, V_{module} is stepwise decreased from 0 to −250 V, and in the second half of the experiment, it is increased back to 0 V. **b** The plot of the minimum transmitted light intensity as a function of ΔV for the first half of the experiment (solid circles) and that for the second half of the experiment (open triangles). The red curve represents a theoretical fit to the data of the solid circles for $\Delta V < -67$ V. Error bars are added to the solid circles at $\Delta V = -117$ V, and −167 V, and the open triangles at $\Delta V = -17$ V, −67 V, and −117 V. **c** The values of ΔV and ΔV_{Si} at the time instant "A" in (**a**). Positive ions are accelerated toward the exposed metallic components, while no charges are accelerated toward the top silicon layer. **d** The values of ΔV and ΔV_{Si} during time region "B" in (**a**). Positive ions are accelerated toward the exposed metallic components due to the negative ΔV, and electrons are pulled toward the top silicon layer due to the positive ΔV_{Si}. The Coulomb repulsion from the charges in the metallic components near the silicon photonic waveguide chip slow down the flow of electrons to the waveguide, causing a relatively slow increase in the transmitted light intensity.

While the basic capability of monitoring ΔV was confirmed, the following issues should be considered for further improvements: Firstly, there are differences between the sensitivities of different sensor modules, as revealed by the differences between the base levels of the transmitted light intensity at $V_{module} = -100$ V in Fig. 3a, 4a, and 5a. Secondly, although V_{module} was kept at a constant negative value in each of the experiments shown in Figs. 3a, 4a, and 5a, the light intensity did not completely stabilize. Based on the results in Fig. 6a, it takes more than 10 min to reach a stable value. Furthermore, the response speed in the case of voltage steps to more positive voltages is also slow. A gradual decrease was also observed in the latter half of the time region (iii) in Fig. 3a (similar response was observed in Fig. 6). Thirdly, during the recovery process when V_{module} is returned from a negative potential to 0 V, overshoots are randomly observed, as can be seen in Fig. 4a.

These phenomena may be related to the native oxide layer and localized energy states on the silicon waveguide surface. Charges trapped in the oxide or surface states do not contribute to FCA and therefore do not reduce the transmitted light intensity. On the other hand, they contribute to matching the silicon waveguide potential with the V_{plasma} (i.e., bringing ΔV_{Si} closer to 0 V). To improve the overall performance, it is important to elucidate the relationship between the silicon surface and the sensor responses. Surface passivation with SiN may be an effective approach. Furthermore, the development of a module design that improves the interaction between the plasma and the top silicon layer is required. For example, the amount of metallic parts near the silicon photonic waveguide chip can be reduced by directly bonding the fiber to the waveguide. Using a highly conductive adhesive to attach the silicon photonic waveguide chip to the metal plate may also be effective. A silicon chip with a longer waveguide can provide higher sensitivity by yielding greater optical attenuation at smaller ΔV, as expressed by Eq. (2).

Finally, since the ΔV experienced by satellites is negative in most cases, we investigated the response to negative V_{module} values. We confirmed that transmitted light decreases even under positive ΔV in a separate experiment with Ar-ion atmosphere instead of Xe ion, where FCA is caused by electrons instead of holes (see Supplementary Information). It could also be useful to add a function that allows us to distinguish whether ΔV is positive or negative.

The advantages of the presented photonic charge sensor for use in space are that it is sufficiently compact to be mounted on small satellites, that it is resistant to the vibrations experienced during rocket launches (we

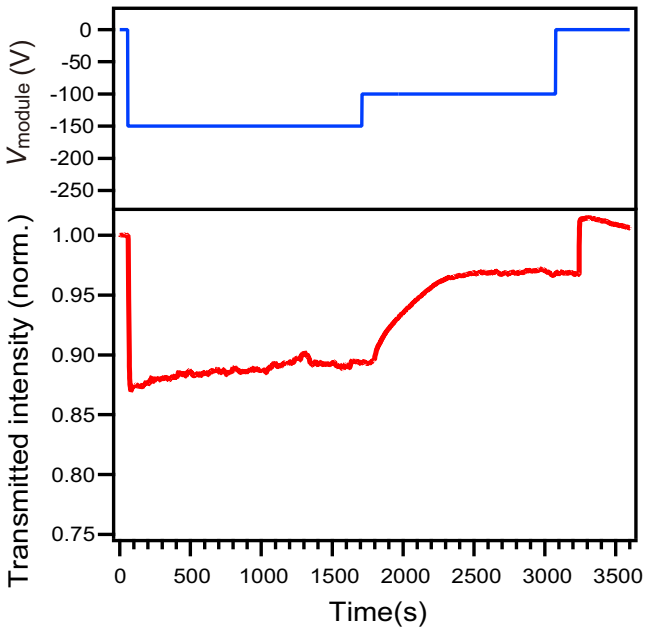

Fig. 6 | Demonstration of monitoring negative ΔV values over a longer period of time. The applied voltage profile (upper panel) and the recorded device response (lower panel).

confirmed this in a separate experiment), and that a high radiation resistance can be expected since the device does not contain a p–n junction (the radiation hardness will be reported in a separate paper). Furthermore, due to the used sensing mechanism, a low energy consumption and a high SN-ratio are expected. The total power requirement of the sensor system, including the light source, photodetectors, and signal processing unit, is estimated to be about 0.1 W. By employing quasi-continuous wave light (i.e., duty-cycled operation), the power consumption can be reduced even further.

Here, we provide an overview of previous approaches for measuring spacecraft potential. Direct potential measurements using the Floating Potential Measurement Unit (FPMU)[42], double-probe techniques[30], and surface electrometers[43] have successfully monitored the potential difference of large spacecraft with an accuracy of better than 1 V. This level of accuracy is superior to that of the photonic charge sensor, even with anticipated improvements in the latter. However, these instruments are inherently large: the FPMU employs four separate probes and the overall system exceeds 1 m in size, while the double-probe method requires wire booms extending more than 10 m from the spacecraft. Surface electrometers are smaller, typically several tens of centimeters, but ensuring radiation hardness is challenging and increases their cost. As a result, the use of these instruments has been limited to large-scale missions.

Indirect approaches combined with numerical simulations have also been explored, for example using particle detectors[44], electron guns[45], and Langmuir probe[46,47]. Particle detectors are typically several tens of centimeters in size and relatively expensive, making them impractical for CubeSat-class missions. The electron-gun approach enables touchless estimation of spacecraft potential and has the advantage of measuring charging levels exceeding 1 kV. However, it requires a dedicated servicing spacecraft equipped with an electron gun. Langmuir probes, which can be reduced to several tens of centimeters, are relatively low-cost and therefore remain a practical option for CubeSat-class spacecraft. However, their accuracy sometimes deteriorates significantly as a consequence of miniaturization, with errors that can reach tens to more than 100%[47]. In summary, compared with conventional techniques, the photonic charge sensor offers advantages in terms of size, cost, power consumption, and radiation resistance.

Monitoring potential differences experienced by spacecraft can help to advance our understanding of ESD failures, and this facilitates the development of effective countermeasures. It is particularly important to measure the potential differences between two distinct locations in the satellite by placing one sensor on the metallic outer shell and another on an insulating material, such as a solar panel. Equipping more satellites with sensors like the presented photonic charge sensor should thus help to reduce ESD failures and also provides more data about space environments[48].

Moreover, several tens of photonic charge sensor modules can be installed on large spacecraft such as the ISS. Each sensor requires less than 0.1 mW of excitation light, and therefore, by using a fiber splitter, the output from a single light source can be distributed to several tens of sensors. Moreover, this sensor is expected to function not only in LEO but also in other environments where ambient plasma is present. Based on the operating principle and the present experimental results, we anticipate that the sensor could also operate in GEO and possibly on the lunar surface.

In the actual LEO environment, the dominant plasma species are H and O, with minor contributions from N and He. The results obtained with Xe plasma showed good agreement with those obtained using Ar ions, as presented in the Supplementary Information. Furthermore, we performed additional experiments in which the position and orientation of the sensor were varied inside the chamber to change the plasma density around the module, and no significant differences in the transmitted light attenuation were observed. In these experiments, the plasma density is expected to have differed by more than one order of magnitude. These results suggest that the photonic charge sensor will reproduce the present experimental behavior in LEO with an agreement of roughly 70%.

To accurately measure the spacecraft potential in space, it is necessary to take into account the influence of temperature. The temperature variation of the silicon photonic chip affects both the refractive index (n_{wg}) and the σ_{FCA} in Eqs. (2) and (3). The former shifts the guided wavelength band of the waveguide, while the latter changes the α_{FCA}. When the chip temperature increases by 100 °C, n_{wg} increases by only about 0.5%, whereas σ_{FCA} increases by approximately 40% (correspondingly, α_{FCA} in Eq. (2) increases by 40%)[49]. Therefore, the transmitted light attenuation ($I_{\Delta V}/I_0$) should depend on the temperature. Monitoring the module temperature is thus necessary to compensate for errors in estimating ΔV.

Methods

Module design

The module illustrated in Fig. 2a was produced by Optoquest Co., Ltd, a photonics foundry specializing in the fabrication and development of advanced optical components. The optical insertion loss of the module was measured to be approximately 15 dB. To ensure no outgassing within the vacuum chamber, a bare single-mode fiber was employed. The silicon chip was mounted onto a metal plate using an adhesive. To prevent contamination of the silicon chip surface, a protective cover was installed on the module. For the experiments depicted in Fig. 2c, this cover was removed.

Photonic chip fabrication

The silicon photonic crystal chip was fabricated on a 300-mm wide silicon-on-insulator wafer by a CMOS-compatible process[40]. The 225-nm-thick top silicon layer is naturally doped with P-type boron at a low concentration of about $1.0 \times 10^{15}\,cm^{-3}$. The photonic crystal patterns were defined using a 193-nm ArF excimer laser immersion scanner and were transferred onto the top silicon layer by dry-etching procedure. The wafer was diced into 800×2000 μm chips by stealth dicing. After cleaning of the surface, the BOX layer was selectively removed using 48% hydrofluoric acid to form an air-bridge structure (see Fig. S2b).

Experimental method

The excitation light shown in Fig. 2c is a broad light with a center wavelength of 1550 nm and a full width at half maximum of 41 nm. A superluminescent diode (SLD, Thorlabs SLD1550PA40) was used as the excitation light source. The light from the SLD was spectrally shaped using an optical tunable filter (OTF, Optoquest WTFA-1580-3-P/F). The excitation light was modulated at 1 kHz using a mechanical chopper and passed through a

polarizer to obtain transverse electric (TE) polarization. This light was transmitted to the module in the vacuum chamber via a fiber feedthrough (Cosmotec). The emitted light from the module was transmitted to the photodiode (Newport model 2011) outside the chamber and the intensity was measured with a lock-in amplifier system (NF LI5630). The background pressure in the chamber was approximately 7×10^{-4} Pa without Xe plasma, and the pressure during the plasma generation was about 2.5×10^{-3} Pa. The experiments were performed at room temperature, 295 K. The temperature increases of the module and the CubeSat was approximately 2 K after 1 h of plasma generation. This gradual temperature rise caused a slight variation in the transmitted light intensity due to the shift in the optical insertion loss of the module.

Data availability

The experimental data that support the plots within this paper and other findings of this study are available from the corresponding author upon request.

Received: 18 February 2025; Accepted: 19 November 2025;
Published online: 02 February 2026

References

1. Zhang, J. et al. LEO mega constellations: review of development, impact, surveillance, and governance. *Space Sci. Technol.* **2022**, 9865174 (2022).
2. Chen, Q. et al. Analysis of inter-satellite link paths for LEO mega-constellation networks. *IEEE T. Veh. Technol.* **70**, 2743–2755 (2021).
3. Lagunas, E. et al. Low-Earth orbit satellite constellations for global communication network connectivity. *Nat. Rev. Electr. Eng.* **1**, 656–665 (2024).
4. Alam, A. et al. Using Landsat satellite data for assessing the land use and land cover change in Kashmir valley. *GeoJournal* **85**, 1529–1543 (2020).
5. D'Errico, M. et al. Observation frequency analysis for multiconstellation radar systems over the Mediterranean Sea. *Int. J. Aerospace Eng.* **2023**, 3209006 (2023).
6. Shen, L. et al. National quantifications of methane emissions from fuel exploitation using high resolution inversions of satellite observations. *Nat. Commun.* **14**, 4948 (2023).
7. Tafazoli, M. A study of on-orbit spacecraft failures. *Acta Astronaut* **64**, 195–205 (2009).
8. Steindorfer, M. A. et al. Space debris and satellite laser ranging combined using a megahertz system. *Nat. Commun.* **16**, 575 (2025).
9. Boley, A. C. et al. Satellite mega-constellations create risks in Low Earth Orbit, the atmosphere and on Earth. *Sci. Rep.* **11**, 10642 (2021).
10. Zhang, J. et al. Long-term evolution of the space environment considering constellation launches and debris disposal. *IEEE T. Aero. Elec. Sys.* **59**, 6124–6137 (2023).
11. Wrenn, G. Spacecraft charging. *Nature* **277**, 11–12 (1979).
12. Garrett, H. B. The charging of spacecraft surfaces. *Rev. Geophy.* **19**, 577–616 (1981).
13. Toyoda, K. et al. ESD ground test of solar array coupons for a greenhouse gases observing satellite in PEO. *IEEE T. Plasma Sci* **36**, 2413–2424 (2008).
14. Choi, H. S. et al. Analysis of GEO spacecraft anomalies: space weather relationships. *Space Weather* **9**, S06001 (2011).
15. Okumura, T. et al. Flashover discharge on solar arrays: analysis of discharge current and image. *J. Spacecr. Rockets* **48**, 326–335 (2011).
16. Fennell, J. F. et al. Spacecraft charging: observations and relationship to satellite anomalies. *7th Spacecr. Charg. Technol. Conf. SP* **476**, 279 (2001).
17. Andersen, A. et al. Perspectives on the distributions of ESD breakdowns for spacecraft charging applications. *IEEE T. Plasma Sci.* **45**, 2031–2035 (2017).
18. Hastings, D. E. A review of plasma interactions with spacecraft in low Earth orbit. *J. Geophys. Res.* **100**, 14457–14483 (1995).
19. Katz, I. et al. Mechanism for spacecraft charging initiated destruction of solar arrays in GEO. *36th AIAA Aerospace Sciences Meeting and Exhibit*. AIAA-1998–1002 (1998).
20. Korth, H. et al. Plasma sheet access to geosynchronous orbit. *J. Geophys. Res.* **104**, 25047–25061 (1999).
21. Garrett, H. B. et al. Spacecraft charging, an update. *IEEE Trans. Plasma Sci.* **28**, 2017–2028 (2000).
22. Carruth, M. R. Jr et al. Experimental studies on spacecraft arcing. *J. Spacecr. Rockets* **30**, 323–327 (1993).
23. Hastings, D. E. et al. Space station freedom structure floating potential and the probability of arcing. *J. Spacecr. Rockets* **29**, 830–834 (1992).
24. Sasaki, S. Plasma effects driven by electromotive force of spacecraft solar array. *Geophys. Res. Lett.* **26**, 1809–1812 (1999).
25. Sarno-Smith, L. K. et al. Spacecraft surface charging within geosynchronous orbit observed by the Van Allen Probes. *Space Weather* **14**, 151–164 (2016).
26. Muranaka, T. et al. Development of multi-utility spacecraft charging analysis tool (MUSCAT). *IEEE T. Plasma Sci.* **36**, 2336–2349 (2008).
27. Wang, J. et al. The ground simulation of spacecraft discharge impacts on the space environment detectors. *IEEE T. Plasma Sci.* **44**, 1247–1253 (2016).
28. Nagatsuma, T. et al. Development of space environment customized risk estimation for satellites (SECURES). *Earth Planets Space* **73**, 1–14 (2021).
29. Pedersen, A. Solar wind and magnetosphere plasma diagnostics by spacecraft electrostatic potential measurements. *Ann. Geophys.* **13**, 118–129 (1995).
30. Tsuruda, K. et al. Electric field measurements on the GEOTAIL satellite. *J. Geomagn. Geoelectr.* **46**, 693–711 (1994).
31. Maurer, R. H. et al. Harsh environments: space radiation. *J. Hopkins APL Tech. D* **28**, 17–29 (2008).
32. Sturm, J. C. et al. Silicon temperature measurement by infrared absorption: Fundamental processes and doping effects. *IEEE T. Electron Dev.* **39**, 81–88 (1992).
33. Liang, T. K. et al. Nonlinear absorption and Raman scattering in silicon-on-insulator optical waveguides. *IEEE J. Sel. Top. Quant.* **10**, 1149–1153 (2004).
34. Takahashi, Y. et al. Detection of ionized air using a photonic-crystal nanocavity excited by broadband light from a superluminescent diode. *Opt. Express* **30**, 10694–10708 (2022).
35. Otsuka, K. et al. Detection of charged particles in a vacuum using a photonic crystal waveguide. In Proc. *Pacific Rim Conference on Lasers and Electro-Optics (CLEO/Pacific Rim)* (IEEE, 2024).
36. Yasuda, S. et al. Detection of negatively ionized air by using a Raman silicon nanocavity laser. *Opt. Express* **29**, 16228–16240 (2021).
37. Fujimoto, M. et al. Control of the sensitivity of the detection of ionized air using photonic crystal waveguides. *Opt. Contin.* **2**, 349–360 (2023).
38. Baba, T. Slow light in photonic crystals. *Nat. Photonics* **2**, 465–473 (2008).
39. Sekoguchi, H. et al. Photonic crystal nanocavity with a Q-factor of ~9 million. *Opt. Express* **22**, 916–924 (2014).
40. Katsura, M. et al. Silicon nanocavity with a quality factor of 6.7 million fabricated by a CMOS-compatible process. *Opt. Express* **31**, 37993–38003 (2023).
41. García-Sánchez, E. R. et al. Agile stage-gate approach for design, integration, and testing of a 1U CubeSat. *Aerospace* **11**, 324 (2024).
42. Aroh, B. et al. Data analysis of the floating potential measurement unit aboard the international space station. *Rev. Sci. Instrum.* **80**, 041301 (2009).
43. Okumura, T. et al. Charging of the H-II transfer vehicle at rendezvous and docking phase. *J. Spacecr. Rockets* **55**, 971–983 (2018).
44. Wilson III, L. B. et al. Spacecraft floating potential measurements for the wind spacecraft. *Astrophys. J. Suppl. S.* **269**, 52 (2023).
45. Hammerl, J. et al. Touchless potential sensing of differentially charged spacecraft using X-rays. *J. Spacecr. Rockets* **60**, 648–658 (2023).

46. Leon, O. et al. The twin-probe method: improving Langmuir probe measurements on small spacecraft. *IEEE T. Plasma Sci.* **50**, 349–359 (2022).
47. Leon, O. et al. Plasma spacecraft interaction codes: model for Langmuir probe operation on small spacecraft. *J. Spacecr. Rockets* **62**, 1044–1052 (2025).
48. Xue, C. et al. Review of sensor tasking methods in space situational awareness. *Prog. Aerosp. Sci.* **147**, 101017 (2024).
49. Svantesson, K. G. et al. Determination of the temperature dependence of the free carrier and interband absorption in silicon at 1.06 μm. *J. Phys. C Solid State Phys.* **12**, 3837–3842 (1979).

Acknowledgements

This work was supported by JST-START (Grant No. JPMJST2111), JST Program for co-creating startup ecosystem (Grant No. KSAC2025_36), and JSPS KAKENHI (Grant No. 21H01373). K.O., T.H., and W.T. acknowledge support from the ICOM Foundation. The authors thank Nozomu Kogiso for support with the preliminary experiment using a vacuum chamber and thank Masao Nakamura for fruitful discussion on space plasma physics.

Author contributions

Y.T. designed and supervised the project. Y.T. designed the photonic charge sensor module. K.O. and W.T. characterized basic optical properties of sensor modules. K.T. and T.M. provided the experimental setup using the vacuum chamber. K.O., W.T., T.H., R.H., and Y.T. performed experiments using a vacuum chamber. All authors contributed to experiments using a vacuum chamber. K.O. and W.T. analyzed the data. K.O., W.T., K.K., T.M. K.T., and Y.T. discussed the results. K.O. and Y.T. wrote the manuscript with assists from K.K. and K.T.

Competing interests

The authors declare no competing interests.

Additional information

Supplementary information The online version contains supplementary material available at https://doi.org/10.1038/s44310-025-00100-6.

Correspondence and requests for materials should be addressed to Yasushi Takahashi.